X-ray absorption spectroscopy measurements of thin foil heating by *Z*-pinch radiation

J. J. MacFarlane,[1] J. E. Bailey,[2] G. A. Chandler,[2] C. Deeney,[2] M. R. Douglas,[2] D. Jobe,[2] P. Lake,[2] T. J. Nash,[2] D. S. Nielsen,[2] R. B. Spielman,[2] P. Wang,[1] and P. Woodruff[1]

[1]*Prism Computational Sciences, 16 North Carroll Street, Suite 950, Madison, Wisconsin 53703*

[2]*Sandia National Laboratories, Albuquerque, New Mexico 87185*

(Received 10 May 2002; published 28 October 2002)

Absorption spectroscopy measurements of the time-dependent heating of thin foils exposed to intense *z*-pinch radiation sources are presented. These measurements and their analysis provide valuable benchmarks for, and insights into, the radiative heating of matter by x-ray sources. *Z*-pinch radiation sources with peak powers of up to 160 TW radiatively heated thin plastic-tamped aluminum foils to temperatures ~60 eV. The foils were located in open slots at the boundary of *z*-pinch hohlraums surrounding the pinch. Time-resolved Kα satellite absorption spectroscopy was used to measure the evolution of the Al ionization distribution, using a geometry in which the pinch served as the backlighter. The time-dependent pinch radius and x-ray power were monitored using framing camera, x-ray diode array, and bolometer measurements. A three-dimensional view factor code, within which one-dimensional (1D) radiation-hydrodynamics calculations were performed for each surface element in the view factor grid, was used to compute the incident and reemitted radiation flux distribution throughout the hohlraum and across the foil surface. Simulated absorption spectra were then generated by postprocessing radiation-hydrodynamics results for the foil heating using a 1D collisional-radiative code. Our simulated results were found to be in good general agreement with experimental x-ray spectra, indicating that the spectral measurements are consistent with independent measurements of the pinch power. We also discuss the sensitivity of our results to the spectrum of the radiation field incident on the foil, and the role of nonlocal thermodynamic equilibrium atomic kinetics in affecting the spectra.

DOI: 10.1103/PhysRevE.66.046416 PACS number(s): 52.25.Os, 52.40.Db, 52.59.Qy, 52.70.La

I. INTRODUCTION

In high-current *z*-pinch experiments at the Sandia National Laboratories *Z* facility, the imploding plasma creates an intense source of radiation which emits up to ~2 MJ of x rays in a ~6 ns full width at half maximum burst with a peak power exceeding 200 TW [1–3]. This radiation source can be used to study physics issues relevant to radiatively heated matter, including: radiation propagation, shock physics, opacity, and photoionized plasmas. These topics are important for inertial confinement fusion, astrophysics, and the understanding of basic processes in both atomic and plasma physics [4–6]. Measurements of this type are important for benchmarking computer codes designed to simulate radiation heating and energy transport through plasmas. Such investigations have been extensively pursued in prior experiments [4–17] using laser-produced x-ray sources. However, the x-ray energy produced at the *Z* facility is roughly two orders of magnitude higher than in present-day laser experiments. The work described in this paper is a first step in examining the exploitation of this large available energy to investigate radiation-heated matter.

A crucial aspect of any radiation-matter interaction experiment is to demonstrate a thorough understanding of the geometry-dependent radiation environment. In the class of experiments considered here, the *z* pinch is surrounded by a cylindrical primary hohlraum. The primary has slots cut out of the side wall to permit pinch radiation diagnostics. A sample covering one of the slots is exposed to both direct pinch radiation and the primary hohlraum reemission. This configuration is analogous to laser hohlraum experiments in which a sample attached to the hohlraum wall is exposed directly to radiation from the laser plasma hot spots and to the hohlraum radiation. However, the spectrum, geometry, and duration of the radiation source are different in laser hohlraum and *z*-pinch hohlraum experiments. It is clearly important to characterize the radiation field in order to fully exploit the *Z*-radiation source.

In this paper we present results from *Z* experiments in which we investigate the time-dependent heating of thin foils exposed to the pinch radiation source. The motivation for this study is to better understand: (1) the radiation characteristics of the *z*-pinch hohlraum; (2) the processes that affect the radiation seen by a sample near the hohlraum boundary; and (3) the response of that sample to the incident radiation field. In these experiments, the heating of thin, plastic-tamped Al foils were monitored by recording time-resolved Kα satellite absorption spectra from the Al, which is a well-established method for measuring properties of radiation-heated materials [12–15]. The pinch served both as the heating source and the backlighter. Two disparate experimental configurations were employed in these experiments to provide distinct benchmarks for simulation codes.

The pinch radiation emission is simultaneously measured using a combination of x-ray diode array (XRD), bolometer, and x-ray pinhole framing camera diagnostics. The radiation incident on the thin foil sample is determined by using the measured pinch radiation as input to a time-dependent view factor code that has an embedded 1D radiation-hydrodynamic model for calculating self-consistent albedos [18]. Time-dependent synthetic spectra, generated by post-processing radiation-hydrodynamics calculations of the foil response to the radiation with a collisional-radiative model, are compared with the measurements. This comparison shows that, up to peak power, good agreement is obtained in each of two experimental geometries with differing hohl-

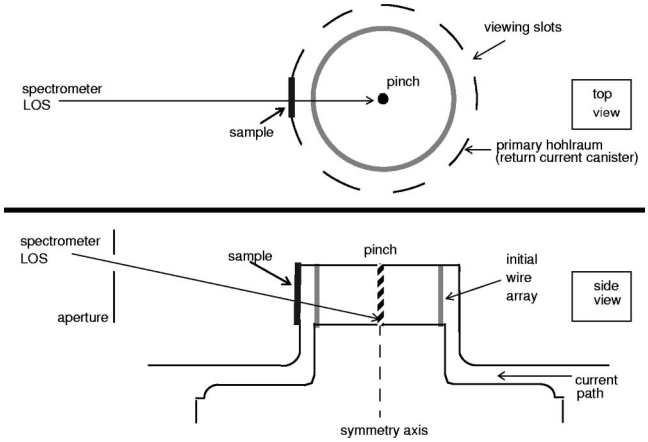

FIG. 1. Schematic illustrations showing top and side views of hohlraum, sample, and diagnostics geometry.

raum and pinch characteristics. After peak power, the synthetic spectra are underionized compared to the data. The consistency as a function of time for the two disparate experimental configurations implies reasonably good understanding of both the pinch radiation field at the sample and the response of the sample to the radiation. Consistency between the foil spectral measurements and the *z*-pinch radiation measurements lends credence to both methods because they both are dependent on the pinch properties, yet they are based on independent diagnostic techniques.

The application of these techniques to successfully diagnose relatively well-understood materials and geometries (planar Al foils) is an important step toward demonstrating the utility of intense *z*-pinch x-ray sources in providing radiation-matter experimental data suitable for benchmarking simulation codes. These techniques will continue to be refined in future experiments [19], such as opacity experiments for radiatively heated materials, radiative heating of relatively low-density gases [20], and experiments utilizing tracer spectral diagnostics in more complex geometries.

The paper is organized as follows. The experimental setup is described in Sec. II. In Sec. III, we discuss our analysis of the radiation incident on the sample foil. The analysis of the foil heating induced by the radiation field is described in Sec. IV, and a discussion of the results is given in Sec. V.

II. EXPERIMENT

The *Z* accelerator delivers an approximately 20-MA peak current to a cylindrically symmetric, 1–2 cm tall, 2-cm-radius annular wire array. The current converts the wires into a plasma that forms a *z* pinch and emits copious x rays. The pinch is surrounded by a slotted canister that provides a current return path and also acts as a primary hohlraum that confines the pinch radiation (Fig. 1). We exploit the radiation by locating a sample in one of the slots, between the pinch and an x-ray spectrometer. The pinch radiation both heats the sample and serves as an x-ray backlighter. This geometry is conducive to performing ''ride-along'' experiments, where the interaction of pinch radiation with various samples can be studied using experiments with an independent main goal, such as the physics of the *z*-pinch formation. Such ride alongs have the advantage that they can examine interesting radiation physics issues without the cost associated with a dedicated experiment. The disadvantages of such experiments are that the radiation may not be optimized for radiation-matter interaction experiments and the sample design and location must be chosen to minimize impact on the main experiment. All the data reported in this paper were acquired using ride-along experiments.

Ride-along experiments can be designed with the sample either attached to the outside wall of the primary hohlraum or located remotely. The former choice maximizes the incident radiation and it provides the most direct comparison with measurements of the primary hohlraum temperature. The disadvantages of attaching the foil to the hohlraum wall are that current may flow through the sample and the magnetic field may affect the sample expansion. Locating the sample remotely from the can wall provides lower radiation intensity, but has the advantages that no current flows through the sample, the magnetic field is much lower, and there is less potential impact on the main experiment. The experiments described here employed samples attached directly to the can wall.

The results from two different *Z* experiments, *Z*419 and *Z*406, are described in this paper. Both experiments used nested (concentric) tungsten wire arrays. The height of the wire array was 10 mm on *Z*419 and 20 mm on *Z*406. The outer array in both experiments consisted of 240 wires with a 40-mm array diameter and a $\sim$7-μm wire diameter. The inner array in both experiments was 20 mm in diameter, with *Z*406 consisting of 240 wires with a 5-μm wire diameter and *Z*419 consisting of 120 wires with a 7-μm wire diameter.

The primary hohlraum configuration is important for radiation-matter interaction experiments because the hohlraum reemission contributes a significant fraction of the total radiation incident on the sample. The primary hohlraum diameter was 5 cm. On *Z*419 this primary hohlraum had 18 diagnostic slots that were 4.4 mm wide, while on *Z*406 there were 9 diagnostic slots that were 10 mm wide. The primary hohlraum walls, ceiling, and floor were coated with gold on *Z*419 in order to enhance the hohlraum reemission. By contrast, on *Z*406 the primary hohlraum walls were boron coated and the ceiling and floor were uncoated stainless steel. The *Z*406 coatings were chosen (for the purposes of the main experiment) to suppress the contribution of primary hohlraum reemission to the radiation measured by the radiation diagnostic suite, as discussed below. The difference in the primary hohlraum coatings is important because it alters the hohlraum reemission contribution to the total x rays heating the sample. The ability demonstrated in this paper to successfully reproduce the sample heating with relatively large and relatively small hohlraum reemission in the two experiments implies that the reemission radiation is reasonably well understood.

The primary purpose of these experiments was to examine the interaction of the pinch plasma with a cylindrical target placed on the axis. The on-axis target was a 5-mm-diameter 4-μm-wall-thickness copper cylinder on *Z*419 and a 5-mm-diameter, 6 mg/cc CH_2 foam on *Z*406. These two experi-

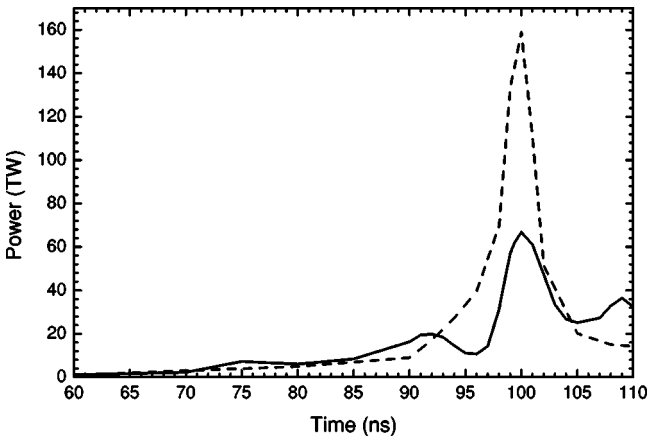

FIG. 2. Pinch power determined from XRD and bolometer measurements for shot Z406 (dashed curve) and Z419 (solid curve), without corrections for Au-electrode reemission.

ments produced about the same total x-ray energy: 1.2 MJ on *Z*406 and 0.9 MJ on *Z*419. However, the difference in the on-axis target produced a radiation time history that was dramatically different. There was a single intense burst of radiation on *Z*406 and a multipeaked time history on *Z*419, as shown in Fig. 2. Despite the significantly different radiation flux histories, we were able to successfully reproduce the evolution of the Al absorption spectra in both cases, thereby giving confidence in the reliability of the technique.

The pinch radiation can be divided into two phases: the run-in and final stagnation. The run-in corresponds to the emission as the annular wire array is compressed from its 2-cm initial radius onto the pinch axis. It lasts for about 100 ns and the brightness temperature rises from approximately 20 eV at the beginning to 50 eV just prior to stagnation. The final stagnation typically creates a 6-ns full width at half maximum (FWHM) x-ray burst with a peak power above 200 TW and a near-Planckian spectrum corresponding roughly to a 200 eV blackbody. The peak radiation powers achieved in the experiments described here were 67 and 160 TW on *Z*419 and *Z*406, respectively. The difference in peak powers is primarily a result of the different target configurations, as opposed to any wall reemission effects. These peak powers were lower than in typical high-power experiments because the primary purpose here was to examine the interaction of the pinch plasma with the on-axis target, not to produce the largest possible x-ray power. In addition to the quasiblackbody radiation, the pinch stagnation also produces tungsten *M*-shell emission in the 2–3-keV photon energy regime. Typically, this *M*-shell emission accounts for roughly a few percent of the total radiation emission. These *M*-shell x rays have not been included in the analysis presented below.

The radiation on *Z* is measured with a diagnostic suite that has been described in detail elsewhere [21–25]. These diagnostics measure the radiation on multiple lines of sight placed at a 78° angle with respect to the pinch axis. Measurements during the run-in phase are accomplished with an absolutely calibrated array of filtered Si diodes that detect radiation from 1–1000 eV photon energies. The spatial distribution of the plasma during the run-in has not been measured and we consequently rely on simulations. The results described here are only weakly sensitive to the exact pinch diameter during this phase. As the pinch stagnates on-axis, the radiation is measured with a combination of an eleven channel filtered XRD array and a three channel bolometer. The pinch diameter at stagnation is measured with time-gated x-ray pinhole cameras. The time history of the total pinch power is inferred by normalizing the integral under the XRD that measures the softest photon energies (140–280 eV) to the bolometers. The XRD or bolometer array views only the lower 58% of the pinch emission, plus a small portion of the primary hohlraum floor. In the determination of the pinch power we assume uniform emission along the entire height of the pinch and that the emission arises from a cylindrical Lambertian source with a Planckian spectrum. Data analyzed with this procedure has been shown to agree with a more complete XRD array unfold and with absolutely-calibrated transmission grating spectrometer measurements to within $\pm 18\%$ [26]. The pinch emission spectrum is inferred by determining the power emitted per unit area from the normalized XRD data and the pinhole camera images and assuming Planckian emission. In other experiments the spectrum determined in this manner was found to agree reasonably well with the spectrum measured by a transmission grating spectrometer [26,27].

The sample heated by the x rays consisted of a CH-tamped Al foil in both experiments. On *Z*419, 8050 Å of Al was sandwiched between 1.42-μm CH and 3.98-μm CH tampers, with the 1.42 μm CH side oriented toward the pinch. This relatively large Al thickness was chosen to permit the observation of both the usual $n=1$ to $n=2$ Al-Kα transitions (n is the principal quantum number), as well as the $n=1$ to $n=3,4,5,6$ transitions. These high-n transitions were successfully observed and the interpretation of them will be presented elsewhere. On *Z*406 the thicknesses were 1.50-μm CH, 2700-Å Al, and 3.96-μm CH, with the 1.50-μm CH side oriented toward the pinch. In both experiments a thinner CH-tamping layer was employed on the pinch side because it was anticipated that the magnetic field produced by the current flowing through the pinch plasma could suppress the foil plasma expansion in that direction.

The absorption spectra used to measure the sample heating were obtained with a time-resolved space-integrated convex crystal x-ray spectrometer. The portion of the absorption spectra recorded near peak pinch power on *Z*419 is shown in Fig. 3. The spectrometer used a potassium acid phlalate crystal with a 26.62-Å $2d$ spacing and bent to a 254 cm radius. The crystal was located 6.48 m from the pinch plasma. The detector was a time-gated microchannel plate (MCP) framing camera with seven Au strip lines that were 1 mm wide and 40 mm long. A 2-ns-FWHM 292 V pulse was applied to the MCP strips in an open circuit configuration with a 275-V dc bias, providing a gain FWHM of approximately 1.3 ns. The interframe time was 3 ns. The detector was isolated from the visible light and ultrasoft x rays in the line of sight by 2 layers of 12.5-μm Be. The detector was positioned 8.6 cm from the crystal and was centered on the 15° Bragg angle ray, providing spectral coverage over the 4–8.5-Å range in first order. The spectral dispersion plane was oriented per-

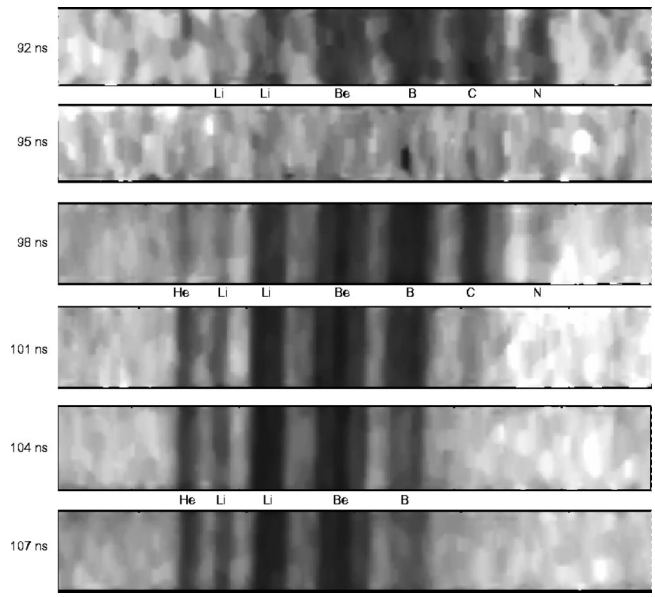

FIG. 3. Measured time-resolved Al-Kα absorption spectra from shot Z419. The times range from 95 to 107 ns, with 100 ns representing the time of peak pinch power, as shown in Fig. 2. The wavelength scale ranges from approximately 7.3–8.5 Å. (See also lineouts in Fig. 10 for wavelengths associated with absorption from each ion.)

pendicular to the plane formed by the pinch axis and the line of sight axis in order to minimize source broadening.

The spectrometer viewed the pinch through the x-ray heated sample as shown in Fig. 1. Thus, the pinch both heats the sample and provides a backlighter for x-ray absorption spectroscopy. The advantages of this configuration are the simplicity of not requiring an independent backlighter, the extreme brightness of the pinch, and the quasiblackbody nature of the pinch radiation over wavelengths longer than approximately 6.5 Å. The pinch brightness enables acquisition of x-ray absorption spectra through relatively thick samples even with the low sensitivity spectrometer configuration used here. The pinch brightness also provides absorption spectra that are not altered significantly by sample self-emission, as confirmed using a time-integrated space-resolved spectrometer in other experiments. The broad wavelength range over which the pinch produces relatively featureless quasiblackbody continuum emission is important because it enables backlighting multiple elements simultaneously. The main disadvantage of using the pinch as a backlighter is that the geometry is constrained. Future experiments using simultaneous backlighting by plasmas independently produced by the Beamlet laser [28] will alleviate this constraint. We also note that it may be possible in future experiments to employ a second spectrometer to directly view the pinch through an uncovered slot [19]. This was not done in the current set of experiments due to resource limitations.

The spectra are recorded on Kodak RAR2484 film placed in contact with the MCP framing camera. The film is developed with a calibrated step wedge and both were digitized with a microdensitometer to enable computer analysis. The analysis began by unfolding the film response using the step wedge. Lineouts were taken separately to average over each MCP frame. A wavelength scale was applied to the lineouts using the instrument geometry, with the 7.757-Å wavelength of the Al-He$_\alpha$ transition as a reference. The accuracy of the wavelength scale is better than 10 mÅ over the 4–8.5-Å range considered here. The spectral resolution was approximately $\lambda/\delta\lambda \sim 450-500$, determined by measuring the widths of emission lines recorded with the same instrument in other experiments. This resolution is consistent with the instrument dispersion convolved with the $\sim$100-μm MCP-resolution element size. We then corrected for the instrument geometry [29], crystal reflectivity [30], and Be filter transmission [31], respectively.

In order to compare the data with the synthetic spectra described below, it is desirable to convert the measured absorption spectrum into the transmission through the sample as a function of wavelength. However, in the present experiments it was not possible to record an unattenuated pinch spectrum. Thus, we could not determine the absolute transmission. Nevertheless, we were able to determine the relative transmission of the Al absorption lines using the following procedure [20]. We first edit each lineout to remove the Al absorption lines. Then we fit the shape of the remaining continuum with a third-order polynomial. This fit represents the approximate incident spectrum from the tungsten pinch plasma attenuated by the continuum (free-free and free-bound) opacity of the sample. We obtained the relative transmission of the Al spectral lines by dividing the original lineout by the fit. We consider such an analysis to be suitable for determining sample heating since the preponderance of the information about the sample condition is included in the relative line intensities, and it is less important to measure the absolute opacities.

III. INCIDENT SPECTRAL FLUX ONTO FOILS

The sample attached to the primary hohlraum wall is exposed to the entire pinch plus reemission from a large portion of the hohlraum floor, ceiling, and walls. In contrast, the pinch radiation diagnostics view only the lower 58% of the pinch plus a small portion of the hohlraum floor. To determine the incident radiation experienced at the sample, we performed view factor simulations, using the experimental measurements of the pinch emission as input.

Our strategy is to first account for the hohlraum reemission contribution to the power measured by the radiation diagnostics, using the view factor simulations described below. This enables us to determine the emission from the pinch alone. Once the radiation emission from the pinch alone is determined, a second set of view factor calculations is performed to determine the radiation intensity at the sample, taking the three-dimensional geometry of the entire radiation source into account. In general this is a time-dependent problem, as the pinch size changes during the run-in. The initial wire radius is 2 cm, a significant fraction of the distance from the final pinch location to the sample. According to simulations the wire plasma moves little during the first 50 ns of the experiment. These factors tend to increase the importance of run-in radiation above what one might

conclude given the low temperature during the run-in compared to the stagnation. This time dependence of the pinch size is less important during the stagnation, since the pinch size change is small compared to the distance between the pinch and the sample. However, the time dependence of the primary hohlraum albedo is important during the stagnation. The hohlraum reemission typically accounts for 25–50 % of the radiation experienced by a sample. This alters the composite spectrum incident on the sample, since the pinch radiation contributes the equivalent of a geometrically diluted 200-eV blackbody, while the spectrum from the reemission varies over a 75–200-eV temperature range, depending on how close the hohlraum segment is to the pinch.

The hohlraum radiation field was simulated using a 3D view factor code that contains an integrated 1D radiation-hydrodynamics (RH) capability. The elements in the view factor grid included the top and bottom plates, the return current wall, the CH-tamped aluminum foil, and the pinch. The code (SYMRAD) [18] computes the time- and frequency-dependent hohlraum reemission by performing independent 1D radiation-hydrodynamics simulations for each surface element in the view factor grid. While the hydrodynamics of each surface element is treated independently, radiation is exchanged between them through the evaluation of their view factors (or configuration factor integrals [32]). One advantage to using an integrated VF-RH approach is that the hohlraum albedos (i.e., the fraction of incident radiation onto a surface that is reemitted) are not input parameters in these simulations. Here, the time-, space-, and frequency-dependent reemission fraction is determined from the RH simulations. Both the incident spectrum onto a surface element and its reemitted spectrum are in general non-Planckian. In addition, this approach does not assume (steady-state) power balance between the incident flux, reemitted flux, and power source terms. Energy stored in a hohlraum plasma element from earlier times can contribute to the radiation field at later times, as can arise when the pinch power changes abruptly. On the other hand, it is important to note that energy is exchanged between the surface elements only by radiation, and energy and momentum exchange by other processes (e.g., conduction and hydrodynamics) are not included in the modeling, such as could be done using a 3D radiation-hydrodynamics code.

The incident radiation flux onto surface element i at time t and frequency ν is given by

$$Q_i(\nu,t)=\sum_j \Gamma_{ij}(t)\ F_j(\nu,t), \tag{1}$$

where $F_j(\nu,t)$ is the flux emitted from surface element j, and $\Gamma_{ij}(t)$ is the configuration factor integral, which is defined as the fraction of energy leaving surface i that arrives at surface j. The time dependence of $\Gamma_{ij}(t)$ in these simulations arises due to the changing radius of the pinch, as the hohlraum surfaces are considered fixed in these simulations. In practice, the time stepping for the individual RH simulations is globally controlled; that is, each RH simulation moves forward in time in a ''lock-step'' manner. Time step constraints are evaluated globally (i.e., based on the change in properties for all RH simulations). A total of approximately 600 surface elements were used to represent the pinch, foil, and hohlraum walls in these simulations. The pinch is modeled as a spatially uniform cylindrical power source that has a time-dependent radius and power determined from experimental measurements (see above). Since the pinch emission power is constrained by measurements, there is no additional contribution to its output power from radiation incident onto it (i.e., it has zero albedo).

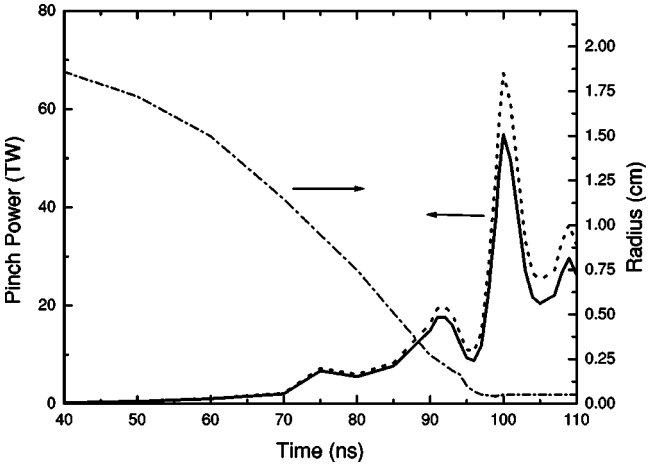

FIG. 4. Dotted curve: Pinch power determined from XRD and bolometer measurements, without corrections for Au-electrode reemission. Solid curve: Pinch power corrected for electrode reemission. Dot-dashed curve: Pinch radius for shot Z419, determined from x-ray framing camera data at 90 ns$<t<$100 ns, and simulation at early times.

The flux reemitted from each surface element is determined from the RH simulation for that element. In each RH simulation, radiation is transported using a multiangle, multigroup radiative transport model based on the short characteristics method [33,34]. In the simulations discussed in this paper, 40 frequency groups were used. Test simulations were performed to ensure the photon energy group structure used was sufficient for this study. Multigroup opacity tables for the materials used in the simulations were generated using the EOSOPA code [35]. Equation of state data were taken from SESAME tables [36]. These opacity and equation of state data were generated assuming local thermodynamic equilibrium (LTE) atomic level populations.

Figure 4 shows the radius and pinch power as a function of time for shot Z419. The power history, uncorrected for reemission, is shown by the dotted curve, while the solid curve represents the pinch power alone. The time axis in all the results presented here has been shifted so that peak x-ray power is at 100 ns. The initial peak (at $t\sim$92 ns) in the pinch power corresponds to the tungsten plasma striking the Cu annulus in this experiment. The maximum power is attained as the plasma stagnates on axis. On Z419 there is a third peak at $t\sim$108 ns which may be due to a second recompression of the pinch plasma. For this shot, the reemission-corrected peak power was 55 TW, while the peak pinch brightness temperature was 202 eV. The correction for hohlraum reemission results in a 23% reduction in power (or $\sim$5% reduction in radiation drive temperature) for shot

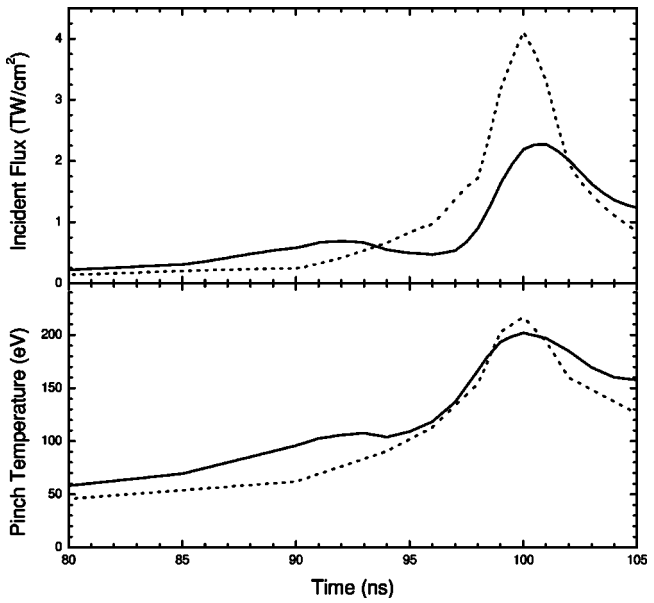

FIG. 5. Top: Calculated incident flux at the foil boundary for shots Z419 (solid curve) and Z406 (dotted curve). Bottom: Time dependence of pinch brightness temperature determined from XRD/bolometer and framing camera measurements for shots Z419 (solid curve) and Z406 (dotted curve), corrected for wall reemission.

Z419. For Z406, the electrode reemission correction to the pinch power was significantly less (~3%), primarily due to the fact that the XRD field of view included only a small portion of the boron-coated hohlraum wall and none of the bottom electrode plate.

Figure 5 (top) shows the calculated frequency-integrated flux onto the CH-tamped Al foils for shots Z419 and Z406. Also shown for each shot (bottom panel) is the time dependence of the pinch brightness temperature (σT_B^4 = pinch power/pinch surface area). Although the peak pinch temperatures are roughly the same for the two shots (202 eV vs 217 eV), the peak incident flux onto the foil is about a factor of 2 higher for Z406. The peak effective drive temperatures, T_D (where σT_D^4 = incident flux) are $T_D \sim 68.6$ and $T_D \sim 79.5$ eV for Z419 and Z406, respectively. Thus, while the peak x-ray powers differ substantially, the differences in effective drive temperature between the two experiments are less pronounced as a result of the larger hohlraum size in Z406. It is also interesting to note that maximum incident flux for Z419 occurs slightly after the peak pinch power (~1 ns), and the pulse width is somewhat broader. This is likely due to energy being stored more effectively in the Au-coated electrodes and side walls, which is reradiated back into the hohlraum over a longer period of time.

The time dependence of the albedo (i.e., the ratio of the reemitted flux to the incident flux) at two locations on the Au-coated bottom plate is shown in Fig. 6. The dotted and solid curves correspond to points located at radii of 0.25 and 1.75 cm, respectively. After the albedos increase monotonically during the first ~70–80 ns of the simulation, they are seen to oscillate in the range of 0.75–1.0. This oscillation occurs due to the fact that the pinch power does not increase smoothly throughout the pulse. When the pinch power increases very rapidly ($t \sim 80$–90 ns and 96–100 ns) the albedos drop, while when the pinch power decreases or is flat ($t \sim 90$–95 ns and 100–104 ns), the albedos increase. This is due to the fact that energy is being stored (in the form of thermal energy) in the hohlraum walls, which can be released at later times. Thus, after peak power the drop-off in incident radiation flux produces the higher albedo.

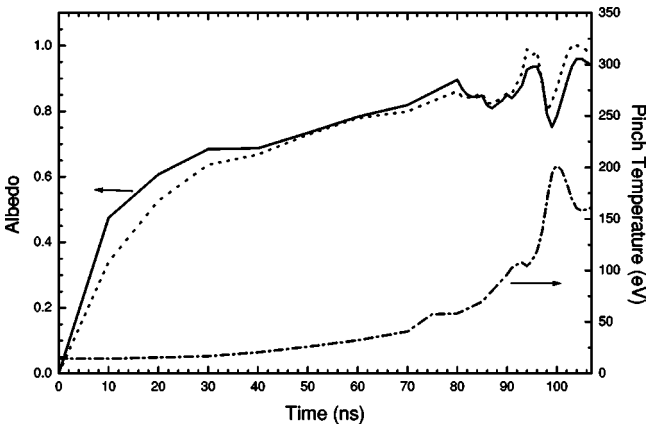

FIG. 6. Time dependence of albedo at two locations on the Au hohlraum bottom plate for shot Z419. Dotted curve: $r = 0.25$ cm. Solid curve: $r = 1.75$ cm. Also shown is the evolution of the pinch brightness temperature (dot-dashed curve).

The spectral distribution of the radiation incident on the foil boundary is composed of two main components: direct radiation from the pinch, and reemitted radiation from the hohlraum surfaces. In our view factor simulations, the radiation from the pinch is modeled as a blackbody emission source. For Z419, roughly 63% of the total radiation incident on the foil at the time of peak pinch power is due to reemitted radiation from the hohlraum surfaces. The corresponding percentage of the radiation due to reemission on Z406 was 42%. Figure 7 shows the calculated spectrum (solid histogram) incident onto the foil boundary at the time of peak

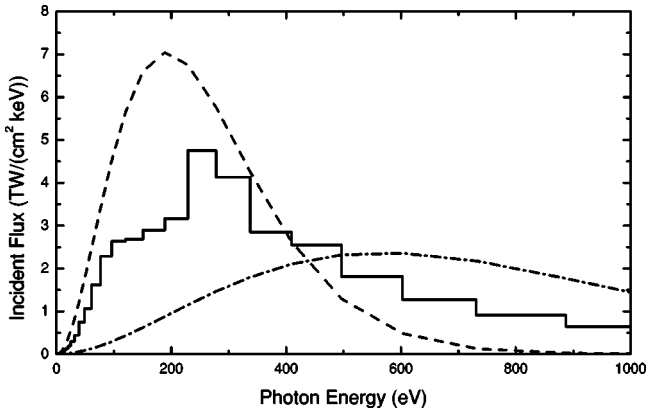

FIG. 7. Calculated incident spectrum onto the CH-tamped Al sample at the time of peak flux for shot Z419 (solid histogram). Two blackbody spectra normalized to give the same frequency-integrated flux are shown for comparison. The dashed curve corresponds to a temperature of $T_D = 67.9$ eV [$T_D = (\text{incident flux}/\sigma)^{1/4}$]. The dash-dotted curve corresponds to the pinch temperature, $T_P = 202$ eV.

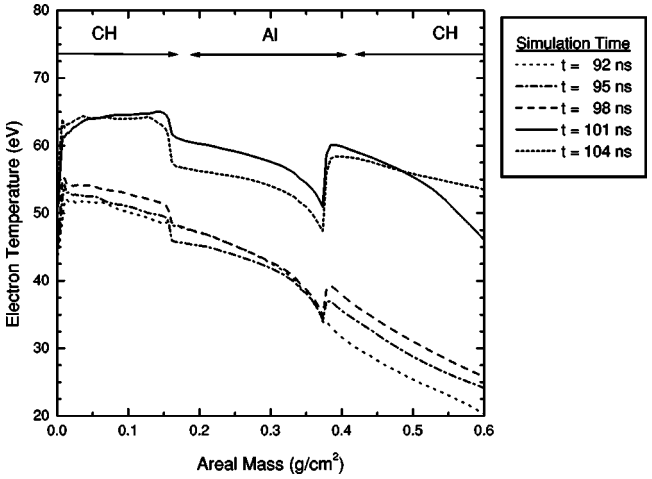

FIG. 8. Calculated temperature distributions in CH-tamped Al foil for shot Z419. Results are shown as a function of areal mass ($\int \rho dr$). The pinch radiation is incident from the left.

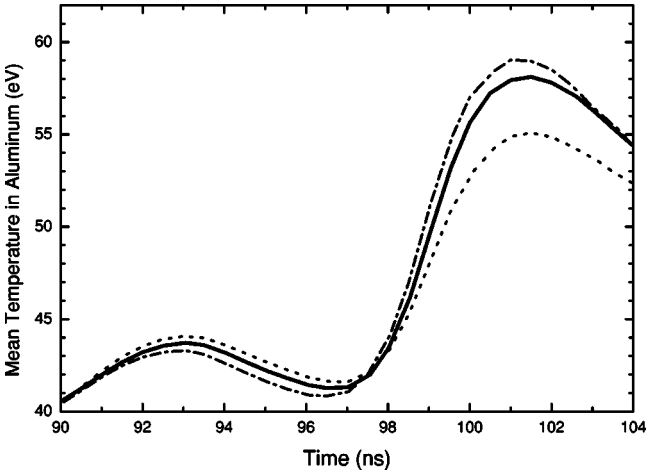

FIG. 9. Calculated mean temperature in the Al layer for shot Z419 from three simulations. All used the same time dependent, frequency-integrated flux, but had different incident spectra. Solid: Simulation with spectra computed from SYMRAD simulation. Dash dotted: Blackbody spectra based on drive temperature. Dashed curve: Diluted blackbody spectra based on pinch brightness temperature.

pinch power (t_{peak}) for Z419. The frequency-integrated flux at this time corresponds to an equivalent blackbody temperature of 67.9 eV. The extent to which this spectrum is non-Planckian can be seen by comparing the total incident spectrum with a blackbody spectrum at the effective drive temperature T_D (dashed line). Here, the total spectrum has a significantly lower flux at photon energies of $h\nu \sim 100-300$ eV, while being substantially higher at $h\nu$ above 600 eV. This is important because for the foil conditions relevant to this experiment ($T \sim$ tens of eV), the Al is heated most efficiently with $h\nu \sim 200-500$ eV photons due to *L*-shell bound-free absorption. Figure 7 also shows a $T = 202$-eV Planckian spectrum (dash-dotted line), corresponding to the pinch brightness temperature at t_{peak}, normalized to the same frequency-integrated flux as the other two curves. It is clear that the spectrum incident on the foil is not adequately described by either the (geometrically diluted) pinch spectrum or the blackbody spectrum defined by the effective drive ''temperature.''

IV. FOIL HEATING ANALYSIS

1D radiation-hydrodynamics simulations are used to compute the heating of the CH-tamped Al foil using the incident power and spectra determined in the Sec. III. Radiation transport and opacity modeling is as described in the previous section. The temperature distribution calculated for the CH-tamped Al foil for Z419 is shown in Fig. 8 at simulation times bounding the peak pinch power. Results are shown as a function of the areal mass to eliminate effects of expansion in the plot. The times shown correspond to those at which spectrometer measurements were recorded. For times ~ 2 to 8 ns prior to peak pinch power ($t \sim 92-98$ ns), the temperature in the Al is ~ 35 to 48 eV, with the higher temperatures being on the pinch-facing side of the foil. Densities in the Al layer are $\sim 2-3\times 10^{-3}$ g/cm^3 (or $\sim 10^{-3}\times$ solid density). During this time period—which corresponds to the period shortly after the $\dot{W}$ strikes the Cu annulus and prior to stagnation—the flux incident on the foil is relatively constant (see Fig. 5). Because of this, the temperature stays fairly constant in time. This effect can also be seen in the Al-Kα spectra (discussed below). As the pinch stagnates on axis, the foil temperature rises to approximately 55 to 60 eV, and then falls at $t > 100$ ns as the pinch power falls.

A relatively thick Al layer (~ 8000 Å) was used in shot Z419. This leads to a temperature gradient across the Al layer at any given time. Thus, a consequence of using a thicker layer is that Kα absorption from a wider range of Al ions is observable. Also apparent in Fig. 8 are fairly distinct changes in temperature near the interface of the CH and Al layers. This occurs because for Al this heating is due primarily to *L*-shell bound-free photoabsorption. For the plastic layers, the heating is due to carbon *L*-shell absorption when the plastic is relatively cool, and *K*-shell absorption at higher temperatures.

The effect of the incident spectral energy distribution on the heating of the foil can be seen by comparing the results from radiation-hydrodynamics simulations which use the same time dependent, frequency-integrated flux onto the sample boundary, but having different incident spectra. Softer spectra are capable of producing higher temperatures in the Al foil because the lower photon energies ($h\nu \sim 200-500$ eV) couple more efficiently with the Al. Figure 9 shows the mean (mass-weighted) temperature in the Al layer from three simulations: the first using the time-dependent spectra predicted from the integrated VF-RH simulations (solid curve), the second using blackbody spectra with the temperature defined by the drive temperature onto the foil (dash-dotted curve), and the third using diluted blackbody spectra with the temperature defined by the pinch temperature, but normalized to have the same frequency-integrated flux as the previous cases (dotted curve). In the case using the non-Planckian integrated VF-RH spectra, the mean electron temperature in the Al layer peaks at 58.1 eV. By com-

parison, the peak temperature is predicted to be approximately 5.5% less ($T=55.1$ eV) when the incident spectrum is based on the pinch temperature. When using blackbody incident spectra defined by the drive temperature onto the foil, the peak temperature is 2% higher ($T=59.1$ eV) than in the non-Planckian case. We note also that the magnitude of these differences is somewhat sensitive to the pinch power. For example, in simulations performed using somewhat higher ($\sim$25%) pinch powers, the temperature differences between the three models are approximately twice as large.

Figure 9 shows that when the *W* plasma strikes the Cu annulus and produces an initial increase in the pinch power to $\sim$18 TW at 8 ns prior to peak power (see Fig. 2), the temperature in the Al layer rises to $T\sim 40-45$ eV. Then, for a period of about 6 ns, the pinch power decreases slightly while the Al temperature exhibits little change. At stagnation ($t\approx 100$ ns) the pinch power rises rapidly to 55 TW and the temperature in the Al increases to about $T\sim 58$ eV.

Aluminum-Kα satellite absorption spectra—which measure bound-bound absorption due to $1s^2\,2s^m\,2p^n \rightarrow 1s^1\,2s^m\,2p^{n+1}$ transitions—were computed for the CH-tamped Al foil by postprocessing results from the radiation-hydrodynamics simulations using a non-LTE collisional-radiative code [37]. In these simulations, steady-state atomic level populations were computed using atomic models consisting of $\sim$300 levels distributed over Ne-like through fully ionized Al. For F-like through Li-like ions, autoionization states with *K*-shell vacancies of the type $1s^1\,2s^p\,2p^q$ and $1s^1\,2s^p\,2p^q\,3m^1$ were included. Fine structure modeling was included for states up to $n=3$ ($n=$principal quantum number), spin-orbit coupling up to $n=5$, and configuration averaging for higher levels. Atomic processes in the collisional-radiative modeling include: collisional ionization and excitation (and their inverse processes), spontaneous emission, radiative and dielectronic recombination, autoionization, and photoionization and photoexcitation. For the latter, contributions to the radiation field included both self-emission from the foil plasma and the incident radiation field onto the foil boundary. Additional details of our Kα spectral modeling for Al have been reported elsewhere [38].

A series of test calculations was performed to assess the importance of various processes affecting the ionization distribution in the Al. These calculations, which used the radiation field and foil conditions typical of times near peak pinch power, indicate that the Al level populations are not adequately described using LTE modeling. For instance, at $\rho=10^{-3}\,\rho_0$ ($\rho_0=$solid density) and $T=55$ eV, the LTE mean charge state for Al is $\langle Z\rangle=9.55$. By comparison, non-LTE optically thin modeling (i.e., no photoionization and photoexcitation) predicts a $\langle Z\rangle=8.85$. By including radiation field effects, both self-emission and an incident radiation field, $\langle Z\rangle$ was predicted to be 9.11–9.24. This is approximately halfway between the LTE and optically thin non-LTE values. In the latter case, gradients in $\langle Z\rangle$ occur in the Al layer because of the spatial dependence of the radiation field. We also note that some of the radiation incident onto the foil is absorbed by the carbon *K*-shell bound-free opacity prior to reaching the Al; thus, the spectrum incident on the Al portion is altered by C absorption.

Figure 10 compares the calculated Al-Kα absorption spectra with experimental measurements from shot *Z*419 at times ranging from 8 ns before ($t=92$ ns) up through 7 ns after peak pinch power, at 3 ns intervals (data at 95 ns are not shown due to low signal level). The simulated spectra are convolved with an instrumental broadening of $\lambda/\Delta\lambda=450$. Up through peak pinch power ($t=100$ ns) the simulated and measured spectra are in good agreement. At $t=92$ and 98 ns, N-like through Li-like Al are clearly seen in both the experimental and simulated spectra, with a relatively small amount of absorption due to He-like Al. These spectra correspond to a period of time where the temperature in the Al changes only slightly (see Fig. 9). At $t=101$ ns, both the experimental and calculated spectra show strong absorption from B-like through He-like Al, modest absorption from C-like Al, and virtually no absorption from lower ionization stages.

Similar results are shown in Fig. 11 for shot *Z*406, where results are shown for times ranging from 6 ns prior to peak power to 6 ns after. In this case, both the measured and computed spectra show a noticeable change in ionization during the time period from 94 to 97 ns. This is due to differences in the on-axis load for these experiments, which results in the lack of a low power ''foot'' for *Z*406 (see Fig. 2). The calculated spectra are in good general agreement with the measurements up to the time of peak power, although appear to be slightly overionized at $t=94$ ns (lack of significant N-like absorption) and $t=97$ ns (less C-like absorption).

At times several ns after peak power in both experiments, the simulations show a lower ionization distribution as compared to measurement. This may be due to the assumption of steady-state atomic level populations in our calculations. In their analysis of laser hohlraum experiments, Merjdi *et al.* [8] showed that time-dependent ionization dynamics can be important in radiation heating experiments, especially so during the plasma cooling phase, where the plasma undergoes recombination. Although the time scales are somewhat shorter in their experiments, it seems very possible that the relatively high ionization distributions that appear in the measured spectra at times several nanosecond after peak power are due to ionization distributions being ''frozen in'' (i.e., recombination times are too long for steady-state assumptions to be valid).

An important issue associated with utilizing spectroscopic diagnostics of this type is the sensitivity of the measured Kα spectrum to uncertainties in the pinch power, which in turn affects the incident radiation flux at the foil. LTE simulations for uniform plasmas, with temperatures and densities typical of those in experiments described here, indicate that, at fixed density, an increase in the electron temperature of 5% leads to an increase in the mean charge state of about 0.2, an amount that should be discernable from measurement. Since the temperature in the absorber depends approximately linearly on the drive temperature ($\sigma\, T_D^4=$incident flux), this change corresponds to a change in the incident radiation power of 22% ($1.22=1.05^4$). This simple analysis provides a very rough estimate of the accuracy needed to constrain radiation powers using Kα absorption spectroscopy.

We note that in the above simulations we have not in-

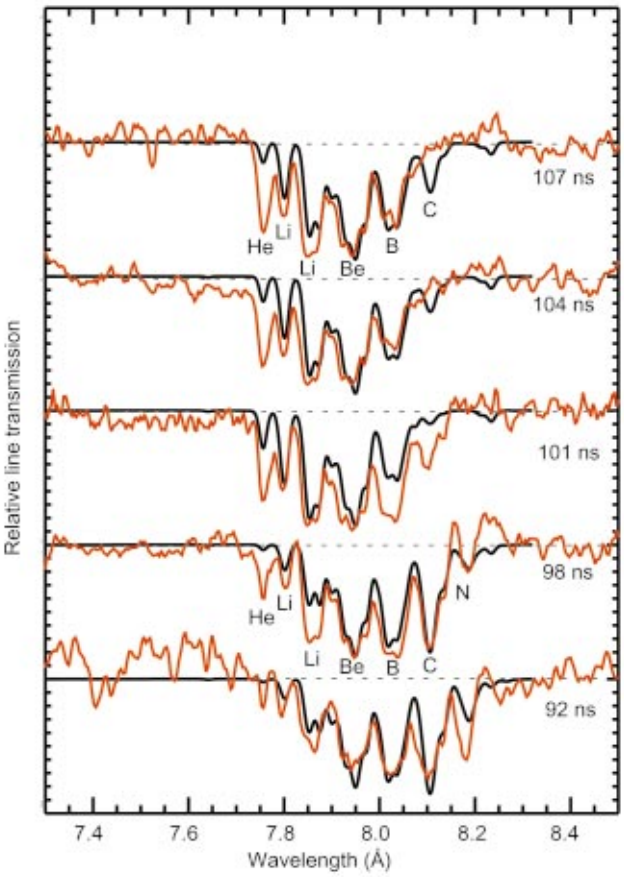

FIG. 10. (Color) Comparison of measured (red curve) and calculated Al-Kα spectra for shot Z419.

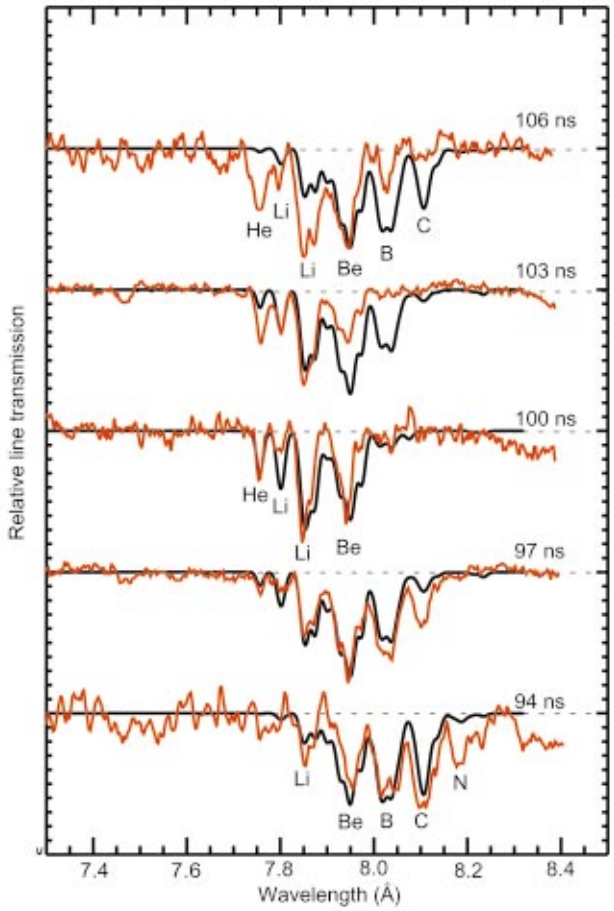

FIG. 11. (Color) Comparison of measured (red curve) and calculated Al-Kα spectra for shot Z406.

cluded direct heating of the foil by the current and the suppression of the foil expansion by the magnetic field. Experiments are now in progress with foils remotely mounted (i.e., located ~ a few centimeter outside of the return current slot), which significantly mitigates the potential impact of these effects. Additional potential inaccuracies in the RH simulations arise due to the assumption of LTE built into the equation of state and multigroup opacity tables. In the future, we will explore utilizing a more accurate inline non-LTE treatment within the RH simulations.

V. SUMMARY

In this paper, we have presented experimental measurements of the time-dependent radiative heating and ionization of planar Al foils exposed to intense *z*-pinch radiation. Using the well-established diagnostic technique of Kα absorption spectroscopy, the heating of thin foils was tracked over a period of ~10–15 ns near the time of peak pinch power. For two different experiments—which had widely disparate peak powers, pinch lengths, surface reemission characteristics, and power histories—the evolution of the Al ionization distribution was successfully measured and modeled. Good agreement between the spectroscopic measurements and simulation was shown up through the time of peak pinch power in both experiments. This analysis indicates that the Al-Kα spectra are reasonably consistent with the pinch radiation powers determined from XRD and bolometer measurements.

Our simulations indicate that the radiation spectrum incident on the foil is significantly influenced by reemission from the surrounding surfaces. For both shots *Z*406 and *Z*419—which utilized stainless steel and Au-coated electrodes, respectively—the incident spectrum contained significant contributions from both direct pinch radiation and surface reemission. Simulations also showed that the heating of the Al foil was sensitive to the spectral characteristics of the incident radiation field. Radiation-hydrodynamics simulations indicate that Al temperatures computed using Planckian incident spectra based solely on the pinch brightness temperature were ~5–10 % lower (depending on the pinch power history) than those obtained using incident spectra determined from integrated view factor or radiation-hydrodynamics simulations.

The consistency between the experimental spectra and simulations suggest it may be possible to deduce pinch radiation characteristics (or more generally *z*-pinch hohlraum characteristics) from Kα absorption spectroscopy of thin foils. This technique could have advantages, for example, in experiments in which it was desirable to achieve high hohlraum temperatures by closing off diagnostic slots in the re-

turn current structure. Another potential advantage of utilizing diagnostic foils to determine radiation field characteristics is that they can be put in locations where the incident radiation views a large solid angle. By comparison, XRD and bolometer measurements typically view direct radiation from a relatively small solid angle.

The analysis methods developed and benchmarked here can be used to design more complex radiation-matter interaction experiments. This includes experiments to study the kinetics of photoionized plasmas, as well as opacity measurements. Also in future experiments, thinner foils will be utilized to minimize temperature and density gradients in the absorbing layer. It is also noted that while Kα absorption spectra provide a direct measure of the plasma ionization state, accurate determination of the temperature requires an independent experimental measurement of the foil density. These issues will be addressed in future experiments.

ACKNOWLEDGMENTS

The authors thank the *Z* accelerator team for excellent assistance in performing the experiments. This work was supported in part by U.S. Department of Energy Grant No. DE-FG03-98DP00250 and by Sandia National Laboratories. Sandia is a multiprogram laboratory operated by Sandia Corporation, a Lockheed Martin Company, for the U.S. Department of Energy under Contract No. DE-AC04-94AL8500.

[1] M. K. Matzen, Phys. Plasmas **4**, 1519 (1997).
[2] R. Spielman *et al.*, Phys. Plasmas **5**, 2105 (1998).
[3] C. Deeney, Phys. Rev. Lett. **81**, 4883 (1998).
[4] R. W. Lee, Fusion Technol. **30**, 520 (1996).
[5] M. D. Rosen, Phys. Plasmas **3**, 1803 (1996).
[6] E. M. Campbell, N. C. Holmes, S. B. Libby, B. A. Remington, and E. Teller, Laser Part. Beams **15**, 607 (1997).
[7] J. A. Koch, C. A. Back, C. A. Iglesias, D. L. McWilliams, R. C. Cauble, E. J. Hsieh, H. N. Kornblum, N. C. Woolsey, J. C. Moreno, A. Asfaw, J. K. Nash, F. J. Rogers, and R. W. Lee, J. Quant. Spectrosc. Radiat. Transf. **54**, 227 (1995).
[8] H. Merjdi, K. Eidmann, C. Chenais-Popovics, G. Winhart, J. C. Gauthier, A. Mirone, and C. A. Iglesias, J. Quant. Spectrosc. Radiat. Transf. **58**, 773 (1997).
[9] H. Merjdi, T. Missalla, T. Blenski, F. Perrot, J. C. Gauthier, K. Eidmann, and C. Chenais-Popovics, Phys. Rev. E **57**, 1042 (1998).
[10] C. Chenais-Popovics, C. Fievet, J. P. Geindre, J. P. Gauthier, E. Luc-Koenig, J. F. Wyart, H. Pepin, and M. Chaker, Phys. Rev. A **40**, 3194 (1989).
[11] F. Gilleron, H. Merdji, M. Fajardo, O. Henrot, J. C. Gauthier, C. Chenais-Popovics, W. Folsner, and K. Eidmann, J. Quant. Spectrosc. Radiat. Transf. **69**, 217 (2001).
[12] T. S. Perry *et al.*, Phys. Rev. Lett. **27**, 3784 (1991).
[13] T. S. Perry *et al.*, J. Quant. Spectrosc. Radiat. Transf. **54**, 317 (1995).
[14] P. T. Springer *et al.*, Phys. Rev. Lett. **69**, 3735 (1992).
[15] C. Chenais-Popovics, F. Gilleron, M. Fajardo, H. Merdji, T. Missalla, J. C. Gauthier, P. Renaudin, S. Gary, J. Bruneau, F. Perrot, T. Blenski, W. Folsner, and K. Eidmann, J. Quant. Spectrosc. Radiat. Transf. **65**, 117 (2000).
[16] C. A. Back, J. D. Bauer, O. L. Landen, R. E. Turner, B. F. Lasinski, J. H. Hammer, M. D. Rosen, L. J. Suter, and W. H. Hsing, Phys. Rev. Lett. **84**, 274 (2000).
[17] C. A. Back, J. D. Bauer, J. H. Hammer, B. F. Lasinski, R. E. Turner, P. W. Rambo, O. L. Landen, L. J. Suter, M. D. Rosen, and W. W. Hsing, Phys. Plasmas **7**, 2126 (2000).
[18] J. J. MacFarlane, J. E. Bailey, T. A. Mehlhorn, G. C. Chandler, T. J. Nash, C. Deeney, and M. R. Douglas, Rev. Sci. Instrum. **72**, 1228 (2001).
[19] J. E. Bailey, G. A. Chandler, D. Cohen, M. E. Cuneo, M. E. Foord, R. F. Heeter, D. Jobe, P. W. Lake, J. J. MacFarlane, T. J. Nash, D. S. Nielson, R. Smelser, and J. Torres, Phys. Plasmas **9**, 2186 (2002).
[20] J. E. Bailey, D. Cohen, G. A. Chandler, M. E. Cuneo, M. E. Foord, R. F. Heeter, D. Jobe, P. Lake, D. A. Liedahl, J. J. MacFarlane, T. J. Nash, D. Nielson, R. Smelser, and W. A. Stygar, J. Quant. Spectrosc. Radiat. Transf. **71**, 157 (2001).
[21] T. J. Nash *et al.*, Rev. Sci. Instrum. **72**, 1167 (2001).
[22] G. C. Idzorek and R. J. Bartlett, in *EUV, X-ray and Gamma-Ray Instrumentation for Astronomy VIII*, edited by O. H. W. Siegmund and M. A. Gummin, SPIE Proceedings Vol. 3114 (SPIE, Bellingham, WA, 1997), p. 349.
[23] G. A. Chandler *et al.*, Rev. Sci. Instrum. **70**, 561 (1999).
[24] R. B. Spielman *et al.*, Rev. Sci. Instrum. **68**, 782 (1997).
[25] L. E. Ruggles, J. L. Porter, and R. Bartlett, Rev. Sci. Instrum. **68**, 1063 (1997).
[26] M. E. Cuneo *et al.*, Phys. Plasmas **8**, 2257 (2001).
[27] M. E. Cuneo, R. A. Vesey, J. H. Hammer, J. L. Porter, L. E. Ruggles, and W. W. Simpson, Laser Part. Beams **19**, 481 (2001).
[28] G. R. Bennett *et al.*, Rev. Sci. Instrum. **72**, 657 (2001).
[29] B. L. Henke, H. T. Yamada, and T. J. Tanaka, Rev. Sci. Instrum. **54**, 1311 (1983).
[30] B. L. Henke (private communication).
[31] B. L. Henke, P. Lee, T. J. Tanaka, R. L. Shimabukuro, and B. K. Fujikawa, At. Data Nucl. Data Tables **27**, 1 (1982).
[32] R. Seigel and J. R. Howell, *Thermal Radiation Heat Transfer*, 3rd ed. (Hemisphere, Washington, DC, 1992).
[33] J. J. MacFarlane, G. A. Moses, and R. R. Peterson, University of Wisconsin Fusion Technology Institute Report No. UWFDM-984, 1995 (unpublished).
[34] G. L. Olson and P. B. Kunasz, J. Quant. Spectrosc. Radiat. Transf. **38**, 325 (1987).
[35] P. Wang, University of Wisconsin Fusion Technology Institute Report No. UWFDM-933, 1993 (unpublished).
[36] S. P. Lyon and J. D. Johnson, editors, Los Alamos National Laboratory Report No. LA-UR-92-3407, 1992 (unpublished).
[37] J. J. MacFarlane, P. Wang, J. E. Bailey, and T. A. Mehlhorn, J. Quant. Spectrosc. Radiat. Transf. **61**, 671 (1999).
[38] J. J. MacFarlane, P. Wang, J. E. Bailey, T. A. Mehlhorn, and R. J. Dukart, Laser Part. Beams **13**, 231 (1995).